

1 **Accurate predictions of iron redox state in silicate glasses: A multivariate approach using**
2 **x-ray absorption spectroscopy**

3 M. DARBY DYAR¹, MOLLY McCANTA², ELLY BREVES¹, CJ CAREY³, ANTONIO LANZIROTTI⁴

4 ¹Department of Astronomy, Mount Holyoke College, South Hadley, MA 01075, U.S.A.

5 ²Department of Earth and Ocean Sciences, Tufts University, Medford, MA 02159, U.S.A.

6 ³School of Information and Computer Sciences, University of Massachusetts at Amherst,
7 Amherst, MA 01003, U.S.A.

8 ⁴Center for Advanced Radiation Sources, University of Chicago, 5640 S. Ellis Ave.,
9 Chicago, IL 60637, U.S.A.

10
11 REVISION 1

12
13 **ABSTRACT**

14 Pre-edge features in the K absorption edge of x-ray absorption spectra are commonly
15 used to predict Fe³⁺ valence state in silicate glasses. However, this study shows that using the
16 entire spectral region from the pre-edge into the extended x-ray absorption fine structure region
17 provides more accurate results when combined with multivariate analysis techniques. The least
18 absolute shrinkage and selection operator (lasso) regression technique yields %Fe³⁺ values that
19 are accurate to ±3.6% absolute when the full spectral region is employed. This method can be
20 used across a broad range of glass compositions, is easily automated, and is demonstrated to
21 yield accurate results from different synchrotrons. It will enable future studies involving x-ray
22 mapping of redox gradients on standard thin sections at 1×1 μm pixel sizes.

23 **INTRODUCTION**

24 It has long been a goal of geoscientists to develop a robust method for microanalysis of
25 iron redox states, and decades of development in the synchrotron x-ray absorption spectroscopy
26 (XAS) community have worked toward this goal. Glasses are of particular interest because of the
27 direct relationship between $\text{Fe}^{3+}/\Sigma\text{Fe}$ and the intrinsic oxygen fugacity (f_{O_2}) of the melt, and the
28 fact that glasses may record the oxidation state of their magma source region and, possibly, the
29 additional effects of magma interaction with the near surface environment.

30 The geological community is especially interested in using XAS to quantify Fe redox
31 states in magmatic and volcanic glasses of varying compositions. Berry et al. (2003) laid the
32 framework for many subsequent studies by using XAS spectra of synthetic silicate glasses with
33 independently-measured $\text{Fe}^{3+}/\Sigma\text{Fe}$ ratios to calculate Fe^{3+} from peak area-normalized centroids in
34 the pre-edge region. Subsequent workers (e.g., Wilke et al. 2005, Cottrell et al. 2009, Lühl et al.
35 2014) also used internal standards to predict redox in glasses. These studies made incremental
36 progress toward development of a more generalized approach because they used only small
37 numbers of standards, so their results were applicable to only limited compositional ranges. They
38 also focused only on the pre-edge portion of the Fe K absorption edge.

39 The challenge now at hand is to improve upon all prior approaches to Fe redox state
40 determinations by exploiting information contained in the entire XAS spectrum, potentially
41 extending into the EXAFS region. For example, Berry et al. (2010) suggest several empirical
42 alternative approaches to calibration of garnet XANES spectra. They report that the average
43 centroid energy of garnet pre-edges is relatively insensitive to $\text{Fe}^{3+}/\Sigma\text{Fe}$, and propose two
44 alternative approaches to $\text{Fe}^{3+}/\Sigma\text{Fe}$ prediction. The first is to use the main absorption edge energy
45 at an arbitrary normalized intensity value of 0.9, and the second employs the ratio of spectral
46 intensities at 7138.4 and 7161.7 eV. This work shows that valuable information is encoded in the

47 main edge and low-energy EXAFS regions.

48 Most recently, Dyar et al. (2012) demonstrated that a multivariate analysis method
49 (partial least squares regression, or PLS) employing the full XAS spectra resulted in dramatic
50 improvements in the accuracy of predicting $\text{Fe}^{3+}/\Sigma\text{Fe}$ in garnets. Results showed that PLS
51 analysis of the entire XANES spectral region yields significantly better predictions of Fe^{3+} in
52 garnets, with both robustness and generalizability, than approaches based solely on pre-edges.
53 Moreover, their PLS coefficients and loadings clearly demonstrate that the vast majority of the
54 useful information in the XANES spectra for predicting $\text{Fe}^{3+}/\Sigma\text{Fe}$ in garnets is found in channels
55 at the main edge and higher. The current study tests the broader applicability of this result on a
56 system of great interest to geoscientists: silicate glasses.

57 This study seeks to overcome the limitations of the previous studies of $\text{Fe}^{3+}/\Sigma\text{Fe}$ by using
58 372 spectra from 60 different bulk glass compositions and comparing information found in the
59 pre-edge region to that in the broader energy range covering the Fe K edge from 7100-7220 eV.
60 We describe a robust model with well-justified error bars that allows determination of $\text{Fe}^{3+}/\Sigma\text{Fe}$
61 over a wide range of silicate glass compositions. Software available from the authors allows this
62 calibration to be used on data from any synchrotron that outputs data in the ubiquitous $\chi\mu$
63 (*.xmu) standard format as output by the ATHENA program (Ravel and Newville 2005).

64 **SAMPLES STUDIED**

65 Compositions of synthetic glass samples studied are shown in **Figure 1** on a plot of total
66 alkalis vs. SiO_2 and as-run compositions are provided in Table 1¹. Starting compositions were

¹Deposit item AM-15-xxxx, Table 1. Deposit items are available two ways: For a paper copy, contact the Business Office of the Mineralogical Society of America (see inside front cover of recent issue for price information). For an electronic copy visit the MSA web site at <http://www.minsocam.org>, go to The American Mineralogist Contents, find the table of contents for the specific volume/issue wanted, and then click on the deposit link there.

67 produced by weighing out appropriate amounts of Alfa Aesar Puratronic oxide and carbonate
68 powders, grinding the mixtures by hand in an agate mortar under ethanol for one hour, and
69 decarbonating (if carbonates were present) at 800°C for 2 hours. Oxide mixes were used directly
70 in the low-SiO₂ experiments without a glassing step. A mixture of sample powder (~100 mg) and
71 polyvinyl alcohol (PVA) was used to adhere the sample to the wire loop. High-SiO₂ runs were
72 first glassed at the appropriate f_{O_2} and the resulting glass was placed on a wire loop (without
73 PVA) and rerun to ensure homogeneity and lack of bubbles.

74 Equilibration experiments were run in a vertical 1-atm gas mixing furnace at Tufts
75 University using the Pt (or Re) wire-loop technique. Re loops were used for low f_{O_2} runs ($f_{O_2} <$
76 QFM [quartz-fayalite-magnetite]). Re wire was used as Fe solubility in the Re is low under the
77 conditions of these experiments (Borisov and Jones 1999). Pt-loops were pre-doped using
78 powders of the identical starting composition for 6 hours at T_{max} and the f_{O_2} intended for the
79 experiment. Glassy material was dissolved off the Pt-loop using a 50:50 mixture of heated HF
80 and HNO₃ and the loop was then used for an experiment. These procedures were followed to
81 reduce but, generally, not eliminate Fe losses to the wire during an experiment. A majority of the
82 samples were equilibrated in multiple f_{O_2} 's including air, CO₂, and at QFM and IW/Mo-MoO₂
83 buffers to vary the resulting Fe³⁺ contents.

84 In addition to those samples, we were fortunate to obtain probe mounts from the wet
85 chemical redox study of Moore et al. (1995), which included many highly silicic samples. Our
86 data set also includes five repeat XAS analyses on a homogeneous bead of volcanic glass from
87 Apollo sample 15081; no Mossbauer analysis is available for that sample, but it is likely to be
88 completely reduced, having formed at IW-0.5 (Sato et al. 1973).

89 METHODS

90 Samples were analyzed during several sessions at beamline X26A at the National
91 Synchrotron Light Source (NSLS), Brookhaven National Laboratory, and beamline 13 ID-E
92 (GSECARS) at the 7 GeV Advanced Photon Source, Argonne National Laboratory. At both
93 beamlines, the beam was focused using mutually-orthogonal Kirkpatrick-Baez mirrors to a $\sim 7 \times 9$
94 μm area (NSLS) or a $1 \times 1 \mu\text{m}$ area (GSECARS). Incident beam energy was controlled by a
95 water-cooled (9°C) Si(311) channel-cut monochromator. At the NSLS, monochromator energy
96 drift was monitored with a magnetite standard that was analyzed before and after every 2-3
97 samples. An energy offset was determined using repeat measurements of the observed pre-edge
98 centroid of the NMNH magnetite standard relative to a reference energy of 7113.25 eV (cf.
99 Westre et al. 1997). At GSECARS, incident x-ray energy was calibrated on the first derivative
100 peak of an iron metal foil standard (7110.75 eV, Kraft et al. 1996) and no energy drift was
101 detected throughout the analytical session. Numerous samples were run at both facilities and the
102 spectra are indistinguishable (Figure 2), indicating that the energy calibrations are comparable.

103 XANES spectra were collected in fluorescence mode using a 9-element high-purity Ge
104 solid-state detector array. Acquisition parameters varied between sessions, but the structure of
105 the Fe K absorption edge was scanned at a sampling resolution of at least 5.0 eV from 7020-7105
106 eV, 0.1 eV from 7105-7118 eV, 0.5 eV from 7118-7140 eV, and 1.0 eV from 7140-7220 eV. The
107 maximum energy of the scan was chosen empirically to avoid any significant remaining
108 oscillations in the absorption spectra to achieve reasonable edge-step normalization.

109 Spectra were processed using the PAXAS (Python Analysis for XAS) software package
110 written for this project by Mirna Lerotic and CJ Carey. The program automates I_0 and edge-step
111 normalization and optional correction for over-absorption (OA). PAXAS works in batch
112 processing mode, taking as input a list of filenames of raw spectra, a list of sample compositions

113 for OA correction, material type (garnet, amphibole, glass), and optional energy shifts for each
114 spectrum. Background removal and edge-step normalization in PAXAS were performed using a
115 linear fit to the pre-edge region (~7025-7085 eV) and a third-order polynomial fit to the post-
116 edge region (~7210-7215 eV) using the algorithm of Ravel and Newville (2005). The optional
117 OA correction uses an adaptation of the FLUO algorithm (Haskel 1999) with absorption cross-
118 sections used to approximate the absorption coefficient from McMaster et al. (1969). Input data
119 files are in the standard $\chi\mu$ (*.xmu) format as output by the ATHENA program (multi-column
120 data of energy bins, fluorescence intensities and incident flux intensities). PAXAS assumes that
121 input data has already been corrected for detector dead-time. The software is configured to
122 output predicted %Fe³⁺ using the optimal algorithm described in Dyar et al. (2012) for garnets,
123 Dyar et al. (submitted) for amphiboles, and this paper for glasses, and is available from the
124 authors.

125 Four variations of data input were employed: pre-edge data only vs. the full spectra, and
126 corrected for OA vs. uncorrected. Each of these four data sets was tested using two multivariate
127 techniques. The first is partial least squares regression (PLS), which calculates components that
128 maximize the covariance between the feature and response matrices (Wegelin 2000). It is
129 especially well suited for problems with many highly correlated features and multiple responses
130 (Kalivas 1999). PLS sequentially chooses directions, or components, of maximal covariance
131 from the feature matrix, \mathbf{X} , and the response matrix, \mathbf{Y} , to determine the model coefficients using
132 a two-step process. The first step is the shrinkage step, in which the shrinkage penalty determines
133 the number of factors to be included in the regression. This shrinks the feature matrix by
134 projecting it from the original p -dimensional space into a smaller q -dimensional vector space. In
135 this project, $p = 600$, the number of channels at which the signal is measured, and q , the number

136 of components, is either allowed to vary from 1-10 or held constant at $q = 6$ in this study. The
137 second step follows ordinary least squares by regressing the response (here $\text{Fe}^{3+}/\square\text{Fe}$) on the
138 components generated in the first step to minimize the residual sum of squared error.

139 The second multivariate technique tested was lasso regression, which is an ordinary least
140 squares regression model with an l_1 penalty on the model coefficients to induce sparsity (Hastie
141 et al. 2009). It produces a sparse model by shrinking some coefficients and setting most other
142 coefficients to zero. It is assumed that a smaller subset of the predictor variables is driving the
143 prediction results. Thus, other coefficients can be excluded from the model (i.e., set to zero) with
144 no significant performance loss. This reduces a sizable, largely uninterpretable model to a sparse,
145 more interpretable model. The lasso adds a regularizer to ordinary least squares to prevent the
146 model from overfitting the training data. It performs automatic feature selection by constricting
147 non-informative feature coefficients to zero. For problems with many features, the lasso can
148 eliminate noisy features that may otherwise hinder the model. These parsimonious models have
149 shown to be effective in many types of chemometric models (Filmozer et al. 2012). The lasso has
150 one hyperparameter, α , that controls the constriction level of the coefficient vector β .

151 The open-source machine learning Python library Scikit-learn (Pedregosa et al. 2011)
152 was used to train and test all models. Accuracy was evaluated using leave-one-out cross-
153 validation and calculated using the root mean square error of prediction (RMSEP), which is in
154 the units of absolute $\% \text{Fe}^{3+}$.

155 RESULTS

156 Results of the 12 permutations on multivariate analyses are given in **Figure 3**: six models
157 using the full spectrum (lasso, PLS with q floating, and PLS with $q = 6$ either with or without the
158 over-absorption correction) and the same six using only the first 120 channels that comprise the

159 pre-edge region. The PLS models with q held constant at 6 are very similar to those in which q
160 was allowed to float. In fact, for both full-spectrum models the floating q converged on a value
161 of 6, the same as the value held constant. The pre-edge models converged on $q = 5$ when that
162 parameter was allowed to vary, but the RMSEP is very similar. We conclude that models with q
163 = 6 are most broadly useful.

164 Overall, the pre-edge-only prediction models yield uniformly inferior results, with the
165 lasso performing slightly better than the PLS models. The full spectrum models all have
166 significantly smaller (better) RMSEP values and the R^2 values of those predictions when plotted
167 against Mössbauer %Fe³⁺ are >0.94. For the 600-channel models, the lasso performs the best,
168 with RMSEP = 3.55 for samples without the over-absorption correction, and ± 3.59 for corrected
169 data. On the basis of these results, the two lasso models will be used in the PAXAS software
170 package; errors on prediction of %Fe³⁺ in glasses can be cited as ± 3.6 for either model.

171 Our data also provide an opportunity to check the applicability of our model to data from
172 two facilities. **Figure 4** shows plots of predicted vs. measured %Fe³⁺ for the two lasso models,
173 with different colors for data from NSLS and APS. There is no appreciable difference between
174 the two data sets, which were acquired on overlapping sets of samples.

175 **Figure 5** shows the results of the models in graphical format. All data are plotted in blue
176 for the full spectra (top panels) and the pre-edge region only. For the lasso models, lasso
177 coefficients are indicated as vertical red lines; selected channels (energies) are indicated by the x
178 axis and the magnitudes of those coefficients are indicated by the length of the bar and the end-
179 point relative to the right-hand y axis. Only a few coefficients are located in the energy region
180 corresponding to the pre-edge signal, indicating that the bulk of information in the spectra about
181 Fe valence state is found in the main edge and EXAFS regions. The same trend is observed to

182 some extent in the PLS model loadings and coefficients. In contrast, the pre-edge models
183 (bottom panels in Figure 5), while less accurate, are remarkably sparse. Note that although the
184 pre-edge centroids have negative rather than positive PLS coefficients (bottom panels of Figure
185 5), that does not they do not influence the predictions. In general, the magnitudes of PLS
186 coefficients are much informative that their signs.

187 **IMPLICATIONS**

188 There is great diversity in standards and methods used by different research groups for
189 prediction of $\text{Fe}^{3+}/\square\text{Fe}$ in glasses, and this has resulted in a general lack of consistency and
190 accuracy across different studies. This work provides a broadly-applicable and widely accessible
191 method that is easily implemented using standard XAS file formats and does not require time-
192 consuming fitting of pre-edge features. Moreover, data from previous studies can easily be re-
193 analyzed to assess the reliability of existing numbers. The new calibration should ensure that
194 cross-comparisons can be made among researchers and synchrotron facilities with known
195 accuracy.

196 Moreover, the automated nature of this technique and its optimal performance from the
197 lasso sparse prediction method open the door to the long-awaited possibility of creating maps of
198 Fe^{3+} at high resolutions. The lasso calibration uses ~ 100 of the 600 channels acquired in this
199 study. Even if adjacent channels are included in a data-acquisition protocol, the time needed for
200 analyzing a single spot will be halved. At ~ 45 seconds per location (including moving the
201 sample) and $1 \times 1 \mu\text{m}$ resolution, it will be possible to create a map of Fe^{3+} on a $50 \mu\text{m}$ glassy area
202 in a thin section in ~ 35 hours. Understanding redox gradients in silicate glasses should provide
203 exciting new insights into magmatic processes at microscales.

204 **ACKNOWLEDGMENTS**

205 We are grateful to Gordon Moore for the loan of the samples from his thesis and 1995 paper.

206 We acknowledge funding from NSF grants EAR-1219761 and EAR-1219850.

207 **REFERENCES CITED**

208 Berry, A.J., O'Neill, H.St.C., Jayasuriya, K.D., Campbell, S.J., and Foran, G.J. (2003) XANES
209 calibrations for the oxidation state of iron in a silicate glass. *American Mineralogist*, 88,
210 967-977.

211 Berry, A.J., Yaxley, G.M., Woodland, A.B., and Foran, G.J. (2010) A XANES calibration for
212 determining the oxidation state of iron in mantle garnet. *Chemical Geology*, 278, 31-37.

213 Borisov, A., and Jones, J.H. (1999) An evaluation of Re, as an alternative to Pt, for the 1 bar loop
214 technique: An experimental study at 1400 degrees C. *American Mineralogist*, 84, 1528-
215 1534.

216 Cottrell, E., Kelley, K.A., Lanzirotti, A., and Fischer, R.A. (2009) High-precision determination
217 of iron oxidation state in silicate glasses using XANES. *Chemical Geology*, 268, 167-
218 179.

219 Dyar, M.D., Breves, E.A., Emerson, E., Bell, S.M., Nelms, M., Ozanne, M.V., Peel, S.E.,
220 Carmosino, M.L., Tucker, J.M., Gunter, M.E., Delaney, J.S., Lanzirotti, A., and
221 Woodland, A.B. (2012) Accurate determination of ferric iron in garnets in bulk
222 Mössbauer spectroscopy and synchrotron micro-XANES. *American Mineralogist*, 97,
223 1726-1740.

224 Dyar, M.D., Breves, E.A., Gunter, M.E., Lanzirotti, A., Tucker, J.M., Carey, C.J., Peel, S.E.,
225 Brown, E.B., Oberti, R., Lerotic, M., and Delaney, J.S. (submitted) Synchrotron micro-
226 XAS analysis of Fe³⁺ in amphiboles. *American Mineralogist*.

227 Filzmoser, P., Gschwandtner, M., and Todorov, V. (2012) Review of sparse methods in

- 228 regression and classification with application to chemometrics. *Journal of Chemometrics*,
229 26, 42-51.
- 230 Haskell, D. (1999) FLUO: Correcting XANES for self-absorption in fluorescence measurements.
231 <http://www.aps.anl.gov/xfd/people/haskel/flu.html>.
- 232 Hastie, T., Tibshirani, R., and Friedman, J., 2009. *The Elements of Statistical Learning*, 2nd Ed.
233 Springer Science, New York, 745 pp.
- 234 Kalivas, J.H. (1999) Interrelationships of multivariate regression methods using eigenvector
235 basis sets. *Journal of Chemometrics*, 13, 1311-1329.
- 236 Kraft, S., Stumpel, J., Becker, P., and Kuetgens, U. (1996) High resolution x-ray absorption
237 spectroscopy with absolute energy Calibration for the determination of absorption edge
238 energies. *Review of Scientific Instruments*, 67, 681-687.
- 239 Lühl, L., Hesse, B., Mantouvalou, I., Wilke, M., Mahikow, S., Aloupi-Siotis, E., and
240 Kanngiesser, B. (2014) Confocal XANES and the Attic black glaze: The three-stage
241 firing process through modern reproduction. *Analytical Chemistry*, 86, 6924-6930.
- 242 McMaster, W.H., Kerr-Del Grande, N., Mallett, J.H., and Hubbell, J.H. (1969) *Compilation of*
243 *X-ray Cross Sections*. Lawrence Radiation Laboratory Report UCRL-50174. National
244 Bureau of Standards.
- 245 Moore, G., Righter, K., and Carmichael, I.S.E. (1995) The effect of dissolved water on the oxidation
246 state of iron in natural silicate liquids. *Contributions to Mineralogy and Petrology*, 120-170-
247 179.
- 248 Pedregosa, F., Varoquaux, G., Gramfort, A., Michel, V., Thirion, B., Grisel, O., Blondel, M.,
249 Prettenhofer, P., Weiss, R., Dubourg, V., Vanderplas, J., Passos, A., Cournapeau, D.,
250 Brucher, M., Perrot, M., Duchesnay, E. (2011) *Scikit-learn: Machine learning in Python*,

- 251 Journal of Machine Learning Research, 12, 2825-2830.
- 252 Ravel, B. and Newville, M. (2005) ATHENA, ARTEMIS, HEPHAESTUS: data analysis for X-
253 ray absorption spectroscopy using IFEFFIT. Journal of Synchrotron Radiation, 12, 537-
254 541.
- 255 Sato, M., Hickling, N.L., and McLane, J.E. (1973) Oxygen fugacity values of Apollo 12, 14, and
256 15 lunar samples and reduced state of lunar magmas. Proceedings of the Lunar Science
257 Conference, 4, 1061-1079.
- 258 Wegelin, J.A. (2000) A survey of partial least squares (PLS) methods, with emphasis on the two-
259 block case. Technical report, University of Washington, USA.
- 260 Westre, T.E., Kennepohl, P., DeWitt, J.G., Hedman, B., Hodgson, K.O., and Solomon, E.I.
261 (1997) A multiplet analysis of Fe K-edge 1s-3d pre-edge features of iron complexes.
262 Journal of the American Chemical Society, 119, 6297-6314.
- 263 Wilke, M., Partzsch, G.M., Bernhardt, R., and Lattard, D. (2005) Determination of the iron
264 oxidation state in basaltic glasses using XANES at the K-edge. Chemical Geology, 213,
265 71-87.

FIGURES AND FIGURE CAPTIONS

266
267
268

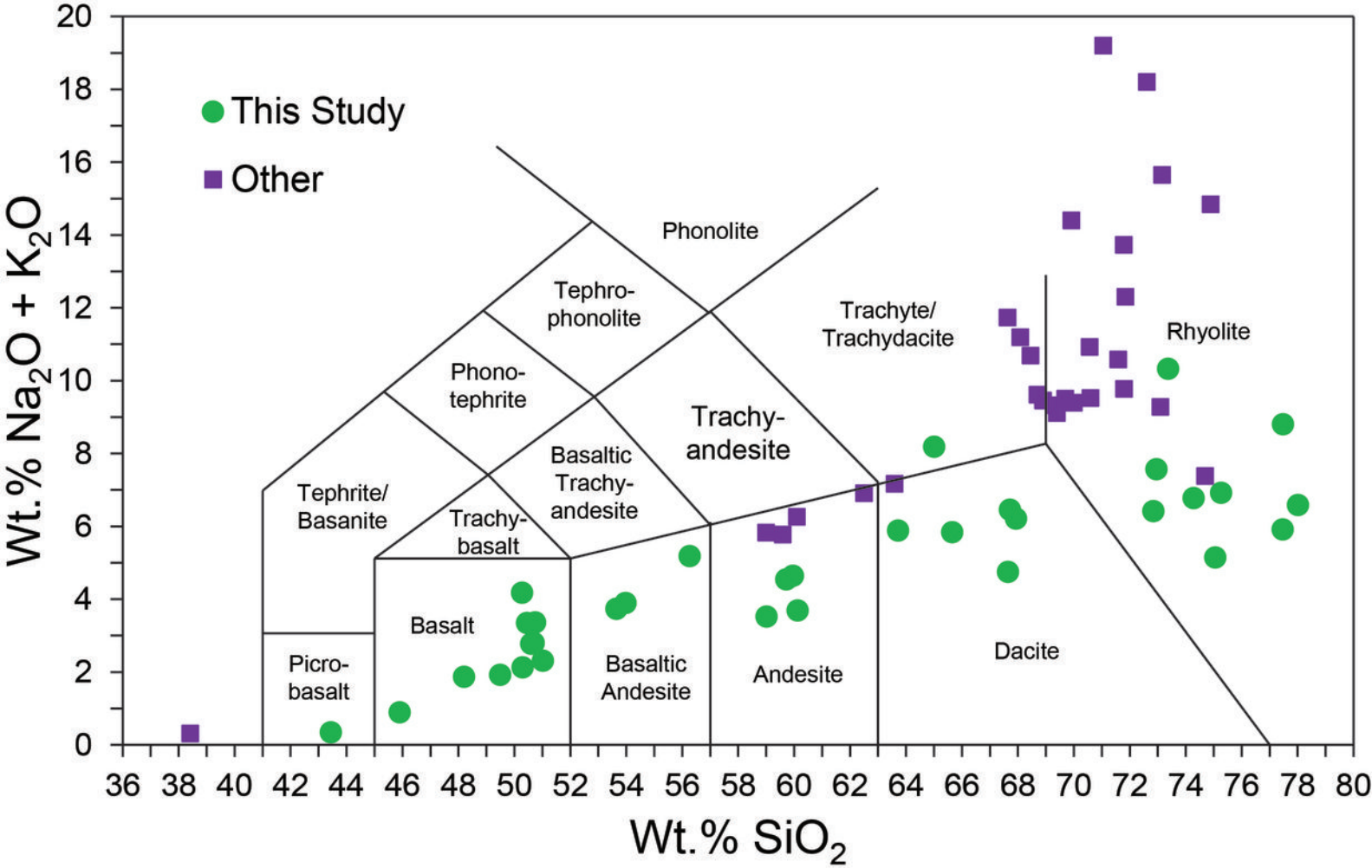
269 **FIGURE 1.** Total alkali vs. SiO₂ diagram showing compositions used for XANES calibration. Green
270 circles indicate samples equilibrated at up to four different f_{O_2} 's, resulting in glasses with nearly the
271 same composition but very different Fe³⁺ contents. Purple squares represent compositions from other
272 studies (see text) for which only a single glass was used. Full compositional information for all
273 standards is given in Table 1.

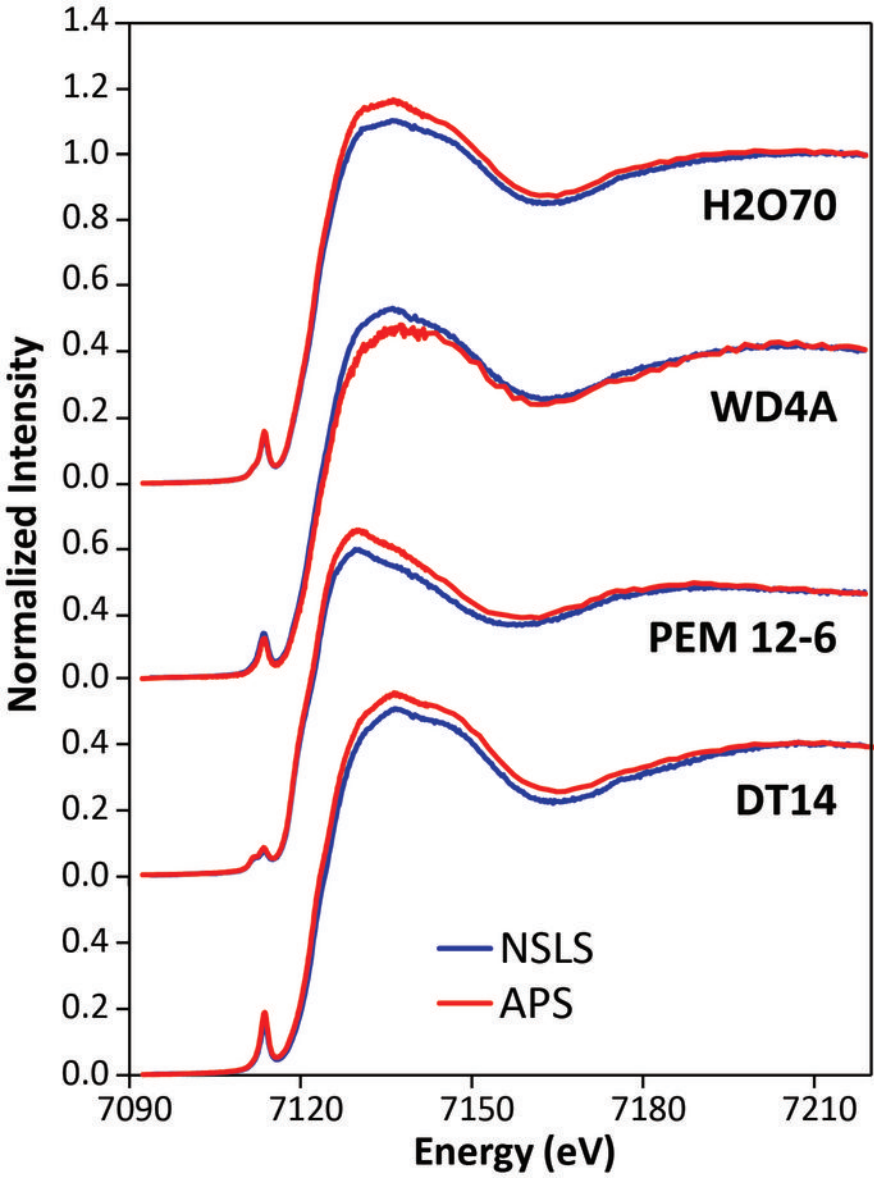
274 **FIGURE 2.** Comparison of over-absorption-corrected XAS spectra acquired at two different
275 synchrotrons: beamlines x26a at the National Synchrotron Light Source at Brookhaven National
276 Laboratory, and the GSECARS beamline at the 7 GeV Advanced Photon Source, Argonne
277 National Laboratory.

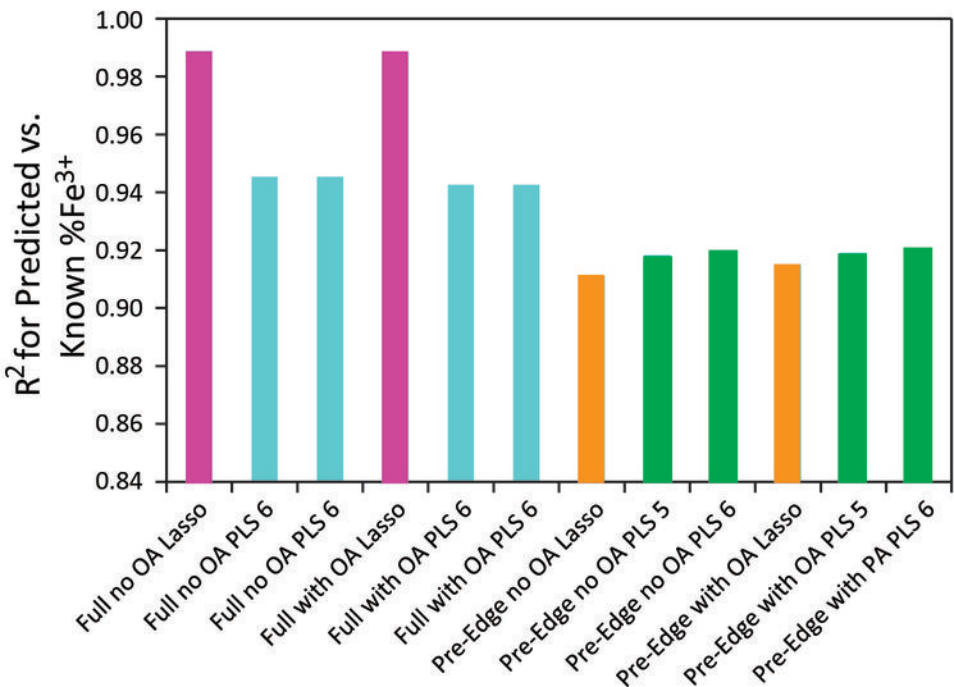
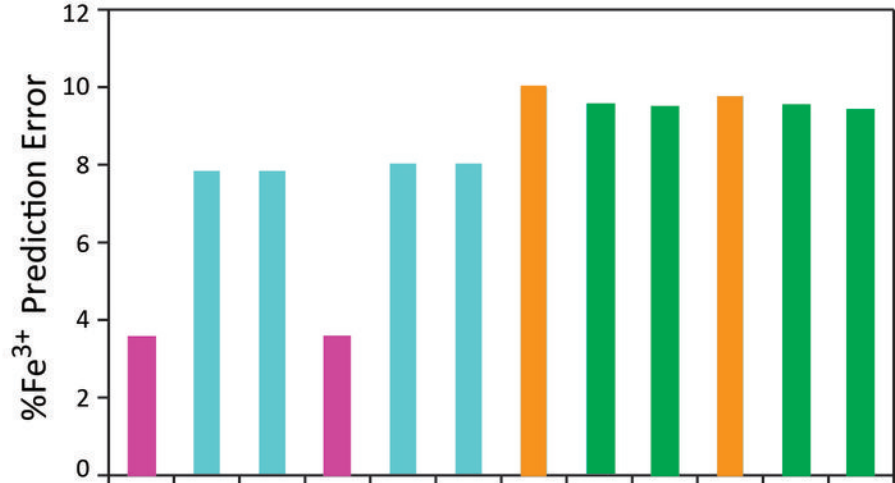
278 **FIGURE 3.** Graphs of leave-one-out cross-validation results from twelve different models showing
279 prediction errors calculated as root mean square errors (top panel) and the R² values for a best-fit line
280 comparing the XAS-predicted %Fe³⁺ values to those from Mössbauer spectroscopy (bottom panel).
281 These results demonstrate that sparse prediction models significantly outperform PLS for this data set.

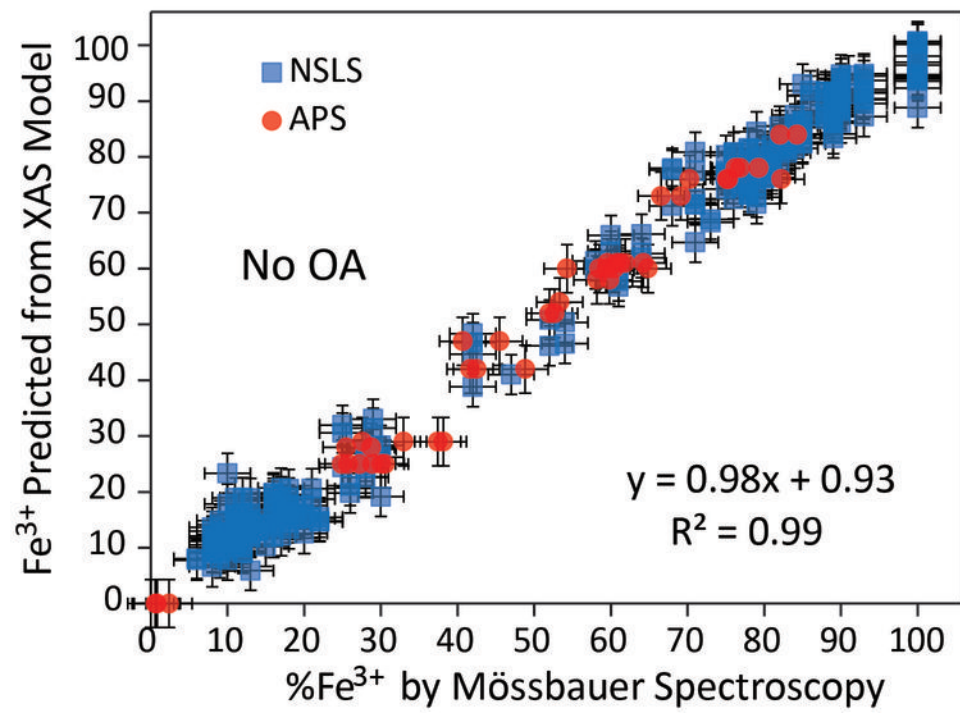
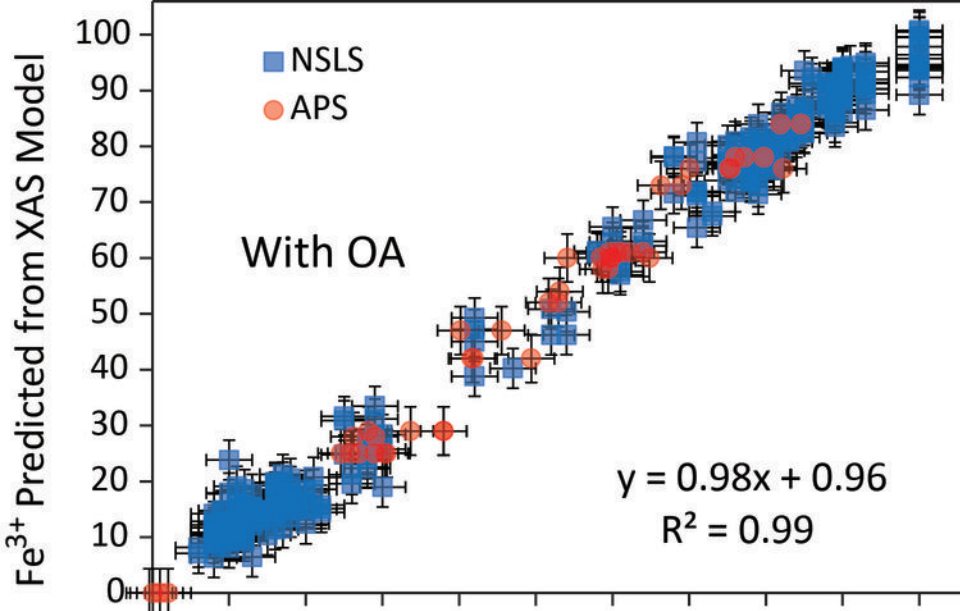
282 **FIGURE 4.** Example plots of predicted Fe³⁺ by the lasso models using the full spectra for data without
283 over-absorption correction (no OA) and with it (with OA). In both cases, the regression line has an R²
284 value of 0.99.

285 **FIGURE 5.** All XAS data in full spectrum and pre-edge-only models are plotted in blue against the
286 locations and magnitudes of lasso coefficients (vertical red lines ending in circles) in square plots and
287 the loadings and coefficients for PLS models (red dashed lines) with $q = 6$, in rectangular plots. The red
288 features indicate the energies at which the prediction of Fe³⁺ is most weighted in the x direction; the y
289 direction shows the magnitude of the coefficient or loading at that energy.

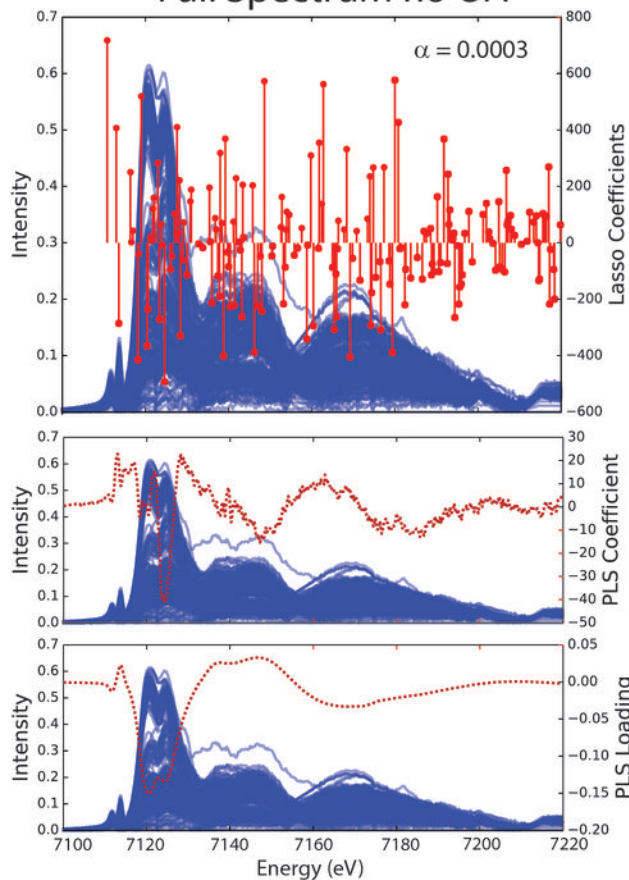




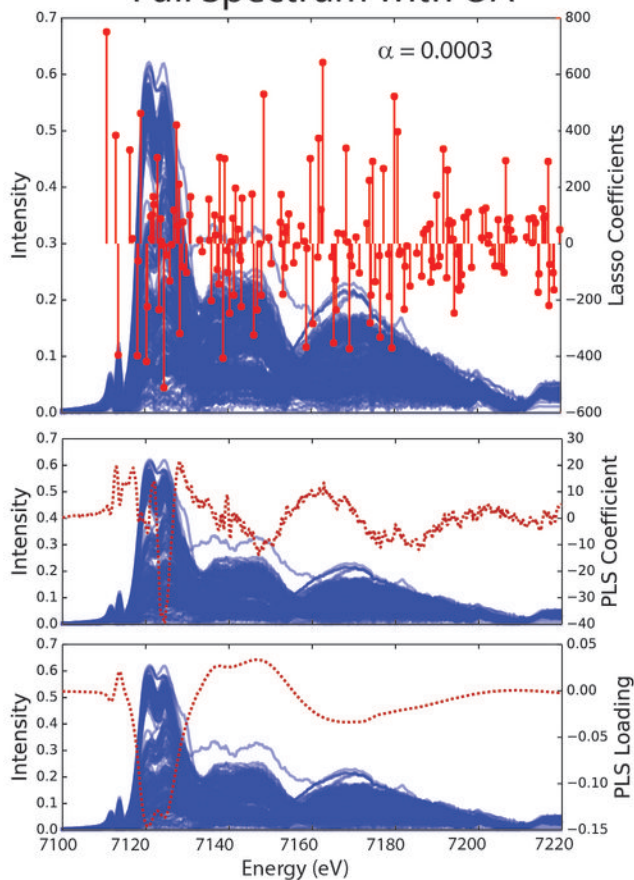




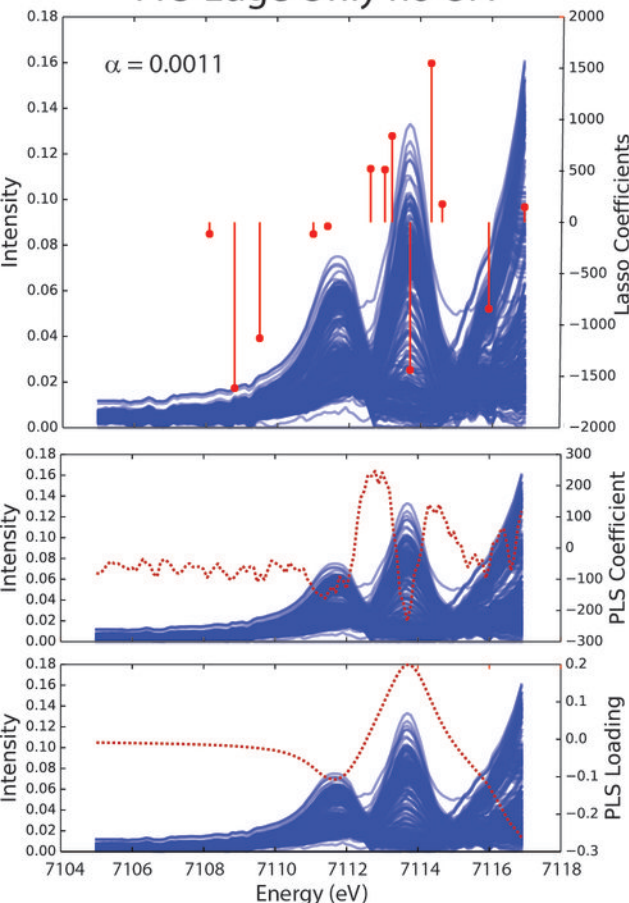
Full Spectrum no OA



Full Spectrum with OA



Pre-Edge Only no OA



Pre-Edge Only with OA

